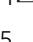





Chemolithotrophy on the Noachian Martian breccia NWA 7034 via experimental microbial biotransformation

Tetyana Milojevic¹, Mihaela Albu^{2,6}, Denise Kölbl^{1,6}, Gerald Kothleitner^{2,3}, Robert Bruner⁴ & Matthew L. Morgan⁵

Multiple lines of evidence indicate an active hydrogeological history of Mars and chemolithoautotrophy-suited environments within its Noachian terrains. As a result, one of the primary aims of upcoming missions to Mars is to search for signs of ancient life. Here we report on laboratory-scaled microbially assisted chemolithoautotrophic biotransformation of the Noachian Martian breccia Northwest Africa (NWA) 7034 composed of ancient (~4.5 Gyr old) crustal materials from Mars. Nanoanalytical hyperspectral analysis provides clues for the trafficking and distribution of meteorite inorganic constituents in the microbial cell. We decipher biomineralization patterns associated with the biotransformation and reveal microbial nanometer-sized lithologies located inside the cell and on its outer surface layer. These investigations provide an opportunity to trace the putative bioalteration processes of the Martian crust and to assess the potential biogenicity of Martian materials.

¹Space Biochemistry Group, Department of Biophysical Chemistry, University of Vienna, A-1090 Vienna, Austria. ²Graz Centre for Electron Microscopy, 8010 Graz, Austria. ³Institute for Electron Microscopy and Nanoanalysis, 8010 Graz, Austria. ⁴Denver Museum of Nature and Science, Denver, CO 80205, USA. ⁵Colorado School of Mines, Colorado Geological Survey, Golden, CO 80401, USA. ⁶These authors contributed equally: Mihaela Albu, Denise Kölbl. ✉email: tetyana.milojevic@univie.ac.at

Recent works heightened interest in the search for biologically driven alterations on Mars and its potential as a habitat for past or present life^{1–4}. Along with an active hydrogeological history of Mars, past chemolithoautotrophy-based habitability was suggested for lacustrine sediments at Gale crater^{1,2}, many instances of phyllosilicate-containing mineral deposits have been reported^{5–10}, and eventually, a thermal habitability window of the early Mars crust was also featured¹¹. A primary aim of the upcoming Mars exploration missions (Mars 2020 and ExoMars) is to search for signs of ancient life. Rovers specifically equipped and well suited to search for signs of life will traverse and explore the surface of Mars, focusing on the Noachian terrains with moisture-rich ancient geological history and mineral springs that could have been colonized by microorganisms. While a range of environments that would have been well suited to support a potential Martian chemolithoautotrophy have been proposed^{1,2,12–14}, our understanding of putative biosignatures to be targeted in Martian materials is still poor. In this connection, a valuable source of information can be extracted from microbial fingerprints of chemolithotrophic life based on Martian materials. Chemolithoautotrophy, as the ancient metabolic form of life^{15,16}, is thought to have enabled the transition of geochemistry into geobiochemistry and served as a biochemical link between the mineral world and the last universal common ancestor^{15,17–19}. Chemolithoautotrophic microorganisms employ an astonishing number of metabolic pathways to extract energy from diverse inorganic electron donors and acceptors²⁰, shaping global biogeochemical cycles. Chemolithoautotrophs that thrive in geothermal springs metabolize inorganic chemicals, a source of energy that provided the most likely habitable niches for life on early Mars. Hydrothermal settings were widespread during the early geologic history of Mars^{21,22} and continued into the late Amazonian period^{23–25}. The tectono-magmatic complexes Tharsis and Elysium have long been known as late Noachian–early Hesperian hydrothermal environments on Mars^{21,22}. Recently, a deep-water hydrothermal environment on ancient Mars (>3.8 Ga (billion years ago)) has been interpreted for Eridania basin based on massive clay-, carbonate-, and sulfide-bearing deposits²⁶. Hydrothermal spring deposits of opaline silica sinter and the case for ancient hot springs in Gusev crater have also recently been reported^{27,28}. Additionally, evidences of past hydrothermal activity in the Martian crust have been derived from the analysis of Martian meteorites^{29,30}. As environmental conditions with hot spring settings were similar on early Earth and early Mars³¹, thermophilic chemolithoautotrophs are under the scope of particular interest³². Moreover, a number of studies have suggested thermophilicity of the last universal common ancestor, implying that life on Earth may have evolved from heat-loving organisms^{33,34}.

Only a few works have been carried out for probing microbial interactions with astromaterials in relation to the study of Martian soil as a possible habitat for microorganisms. Single laboratory investigations on meteorites and Mars regolith analogs have been performed, demonstrating that some iron-oxidizing chemolithotrophs (e.g., *Leptospirillum ferrooxidans*, *Acidithiobacillus ferrooxidans*) could colonize metal-bearing astromaterials and use them as energy sources^{35–37}. The microbial communities, which in situ colonize stony meteorites upon their fall to Earth, have been recently accessed³⁸. Micrometer/nanometer-scale patterns and morphologies at the meteorite surfaces have also been previously investigated in connection with biogenicity criteria for the identification of fossil extraterrestrial life^{39,40}. Using a chondrite meteorite with relatively high iron abundance, we have recently reported chemical analysis of the meteorite–microbial interface at nanometer-scale spatial resolution⁴¹. In order to properly assess Martian relevant biosignatures, it is crucially important to

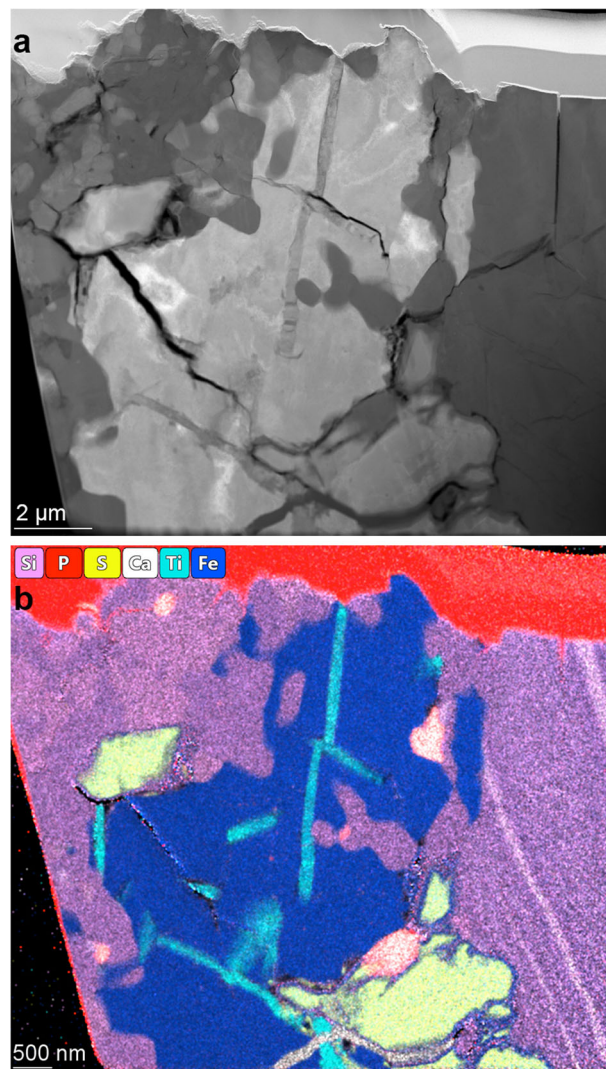


Fig. 1 Images of various lithologic components in the NWA 7034 fragment used in this study. **a** The high-angle annular dark-field (HAADF) scanning transmission electron microscopy (STEM) image of the focused ion beam (FIB) section extracted for STEM analysis from the NWA 7034 fragment used in this study. **b** False-color energy-dispersive X-ray spectroscopy (EDS) composite image of NWA 7034 (Si-magenta, P-red, S-yellow, Ca-white, Ti-cyan, Fe-blue). The full list of detected mineral phases is presented in Supplementary Table 1. The P signal in the region of the Pt layer deposited during FIB sample preparation is due to the overlap of the P-K α and Pt-M α peaks in the EDS spectra. The EDS spectra acquired in STEM mode from both regions are presented in Supplementary Fig. 12.

consider chemolithotrophs in Martian relevant geological and mineralogical settings. Given that returned Martian mineralogical samples are to date inaccessible, Martian meteorites are currently the only samples from Mars available on Earth. We cultivated the extreme thermoacidophile *Metallosphaera sedula*, an ancient inhabitant of terrestrial thermal springs⁴², capable of chemolithoautotrophic growth on terrestrial mineral ores^{43,44} and astromaterials^{37,41}, on the genuine Noachian Martian breccia Northwest Africa (NWA) 7034^{45,46} (Supplementary Fig. 1 and Fig. 1) and investigated microbial–meteorite interactions at nanometer scale. The compositional variety of the polymictic regolith breccia NWA 7034 closely corresponds to the estimated bulk-crust composition of Mars^{29,47,48} and to visible-infrared reflectance spectra of the Martian surface measured from orbit^{29,49}. This brecciated regolith sample represents the

oldest known Martian crust of the ancient crystallization ages (~4.5 Ga)^{29,45,46}, with predominant plagioclase feldspar (38.0 ± 1.2%), low-Ca pyroxene (25.4 ± 8.1%), clinopyroxenes (18.2 ± 4.0%), iron-oxides (9.7 ± 1.3%), alkali feldspars (4.9 ± 1.3%), apatite (3.7 ± 2.6%), and to a lesser amount, chromite and iron-sulfides⁴⁷.

Results and discussion

Growth, elemental ultrastructural, and nanoanalytical spectroscopy analyses. *M. sedula* was cultivated on the Noachian Martian regolith breccia NWA 7034 (Supplementary Fig. 1). The major lithologies of NWA 7034 used in the study were examined by nanometer-scale point analysis of the NWA 7034 thin section using energy-dispersive X-ray spectroscopy (EDS) in scanning transmission electron microscopy (STEM) mode and high-resolution scanning transmission electron microscopy (HR-STEM) techniques. Representative images and corresponding EDS elemental maps (Fig. 1 and Supplementary Fig. 2) indicate the presence of various lithologic components (Supplementary Table 1). The plagioclase-rich areas along with the edges of pyroxene²⁹ were identified on the NWA 7034 thin section (Supplementary Table 1). Some regions were locally enriched with pyrite²⁹ (Supplementary Table 1). Characteristic titanium-bearing ilmenite veins²⁹ were embedded in magnetite clasts (Fig. 1, Supplementary Table 1, and Supplementary Fig. 2). Cl-, P-, and Ca-rich apatite grains²⁶ that exhibit amorphous textures and rounded morphologies were also present (Fig. 1, Supplementary Fig. 2, and Supplementary Table 1). *M. sedula* was capable of chemolithoautotrophic growth on NWA 7034, breaking down its mineral material and solubilizing metals into the leachate solution (Supplementary Fig. 3). Examination of the metal-mobilizing capacities of *M. sedula* by means of inductively coupled plasma mass spectrometry (ICP-MS) analysis showed a release of sulfur (S), along with a leaching of Na, Mg, P, K, and Ca as major elements released from NWA 7034 (Supplementary Fig. 3a). The mobilization of other minor and trace elements (B, Ni, Mo, Li, Rb, Sr, Sb, Cs, and W) was also detected (Supplementary Fig. 3b, c). Viewed from the bioenergetic perspective, pyrite(FeS₂)-rich domains within the proto-breccia clast of NWA 7034²⁹ can provide reduced sulfur and iron species as an energy source for *M. sedula*. Other Fe²⁺-bearing minerals (e.g., ilmenite FeTiO₃; magnetite Fe²⁺Fe³⁺O₄²⁻; pyroxene and plagioclase with Fe²⁺ contributing to the total iron budget) can potentially satisfy the energy demand for *M. sedula* respiration needs, offering the metal ions of a suitable redox potential (Fe²⁺) for its biooxidative metabolic activity. Resulting microbially produced Fe³⁺ species promote further meteorite oxidation and enable the mobilization of metals (including abundant meteoritic Fe³⁺ species) from the solid meteorite matrix into the solution. Such a joint microbially produced and abiotic Fe³⁺ pull acts effectively as an oxidizing agent and facilitate the further process of metal mobilization, thus destroying the meteorite structure. Moreover, manganese biooxidation could also implement in NWA 7034 elemental dissolution mediated by *M. sedula*^{37,43} (e.g., see Mn elemental map in Supplementary Fig. 2 for the Mn content in NWA 7034).

Elemental ultrastructural analysis of *M. sedula* grown on NWA 7034 by using EDS in STEM mode showed that the cells are encased in an Fe-, Mn-, Al-, and P-bearing layer of 50–100 nm thickness that separates intracellular content from its surroundings (Figs. 2, 3 and Supplementary Figs. 4, 5). Fe has a pronounced stronger intracellular signal; however, a substantial portion of Fe is also localized in the cell surface crust (Fig. 2 and Supplementary Fig. 5). STEM inspection of the raw (Fig. 1 and Supplementary Fig. 2) and abiotically treated NWA 7034 material (Supplementary Figs. 6, 7 and Supplementary Table 2) did not reveal the presence of similar cellular assemblages.

Further HR-STEM analysis of *M. sedula* grown on NWA 7034 revealed that encrusted outer layer has a crystalline microstructure with lattice parameters close to different phosphate assemblages: Fe phosphates, Mn phosphates, and Al phosphates (Fig. 3a, b and Supplementary Table 3; see Supplementary Table 4 for the inter-atomic spacing *d*-values). Closely related to *M. sedula* species *Sulfolobus acidocaldarius* also forms Fe phosphates on the cell surface, followed by complete encrustation with Fe phosphates upon incubation in the Fe-rich medium⁵⁰. Mn, Si, and Zn primarily localize intracellularly in *M. sedula* (Supplementary Fig. 4), while N, O, Fe, Na, Mg, S, Cr, and As are evenly dispersed through the cell (Fig. 2, Supplementary Figs. 5, 8, and Supplementary Table 5). The As content has been reported in the meteorite NWA 7533 (paired with NWA 7034)⁵¹. Cells of *M. sedula* were capable of forming budding vesicles (Fig. 4 and Supplementary Fig. 5), similar to the vesicular blebs which we previously observed during the growth of this archaeon on terrestrial minerals^{43,52}. We have also previously observed the formation of *M. sedula* vesicles during growth on the ordinary chondrite NWA 1172⁴¹. Just like the cells, the vesicles are also encased in a Fe-, Mn-, Al-, and P-bearing layer (Fig. 4 and Supplementary Figs. 5, 8). *M. sedula* vesicles have been known to catalyze iron oxidation and promote mineral solubilization under the energy-limited lithoautotrophic conditions⁵³. Such vesicles are biogeochemically active and contain a functional protein machinery involved in iron oxidation, metal release, DNA compaction, and attachment to mineral surface⁵³. Our STEM-EDS analysis detected Fe, Mn, S, Zn, Cr, Na, and As inside the vesicles (Supplementary Fig. 5), indicating vesicular ability to immobilize metals from NWA 7034. Additionally, intensive vesiculation of *M. sedula* cells can function as an efficient mechanism of extracellular metal sequestration by binding with chelating agents (non-specific vesicular proteinaceous material and specific enzymatic detoxification of the metal to a less toxic form)⁵³.

Intracellular nanocrystalline deposits. The NWA 7034-grown cells at the initial stages of biomineralization showed the accumulation of the blade-shaped structures protruding inwards from the cell wall to the cellular interior (Fig. 3c, d and Supplementary Fig. 4a–d). HR-STEM imaging revealed that these blades are associated with nanometer-sized near-spherical aggregates, mainly comprised of Fe, O, Si, and Mn as suggested by STEM-EDS analysis (Fig. 3e, f). These structural nanoassemblages were rather of amorphous nature at the early stages of biomineralization (Supplementary Fig. 4d), most likely representing an initial period of new mineral phase formation. At the late biomineralization stages of cell encrustation (Fig. 4), the cellular interior had heterogeneous, rugged, and coarse character (Fig. 4a and Supplementary Fig. 5), and these metal-bearing nanoassemblages were converted into intracellular crystalline deposits of Fe₃O₄⁵⁴, Mn₃O₄⁵⁵, and mixed Mn_xSi_yO_z-containing phases that could not be identified through the ICSD database (Fig. 4 and Supplementary Fig. 9, see Supplementary Table 4 for the inter-atomic spacing *d*-values). The electron energy loss spectroscopy (EELS) measurements, acquired locally (point analysis with a beam diameter of 1 Å) in STEM mode, demonstrated that the Fe L_{2,3}-edges from the heavily encrusted *M. sedula* cells show a predominant presence of Fe³⁺ species (Fe L₃-edge at ~710 eV, see Fig. 4e and Supplementary Fig. 10). Accomplished microbial Fe²⁺ oxidation^{56,57} leads to cell encrustation and entombment in the mineralized form of different crystalline deposits with the predominant form of Fe³⁺. At the same time, intracellular nanocrystalline deposits have a rather complex character: apart from the aforementioned Fe and Mn oxides, mixed Mn_xSi_yO_z-

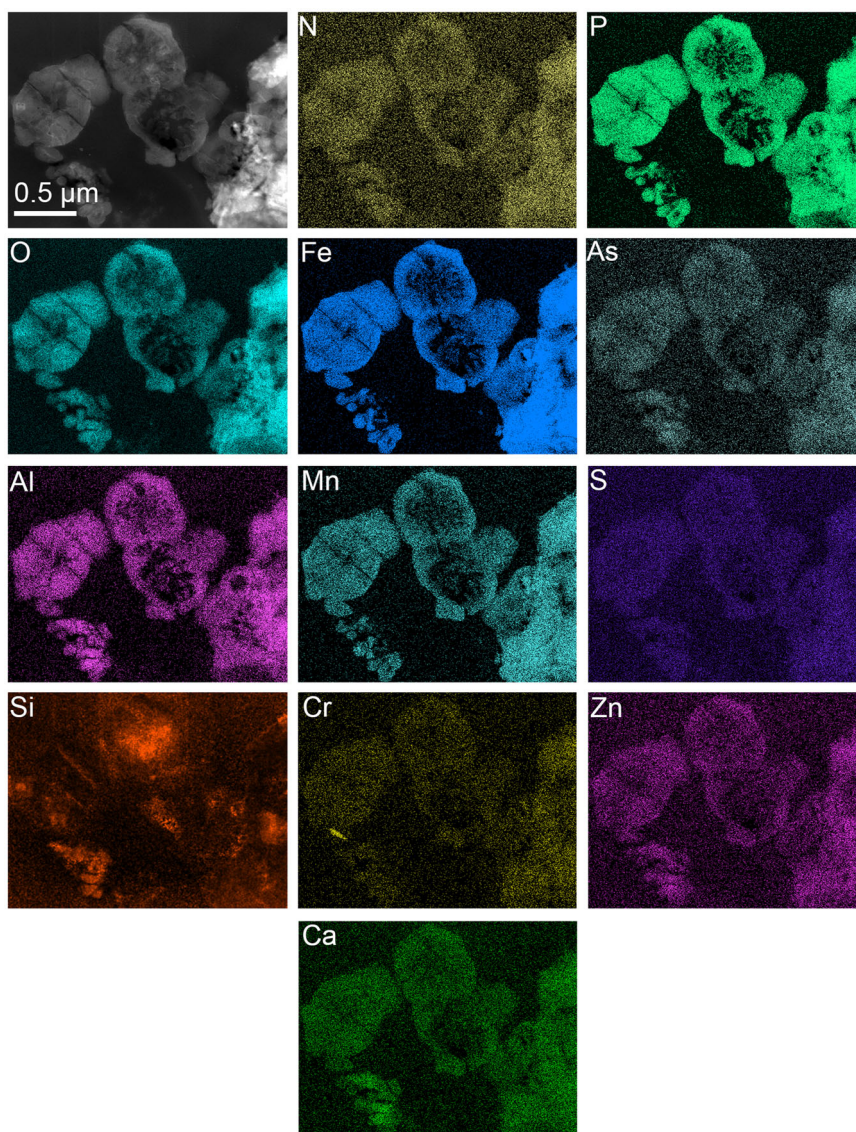


Fig. 2 Elemental ultrastructural analysis of *M. sedula* grown on NWA 7034. The HAADF-STEM image of *M. sedula* cells used for the EDS spectrum image acquisition and corresponding extracted nitrogen (N), phosphorus (P), oxygen (O), iron (Fe), arsenic (As), aluminum (Al), manganese (Mn), sulfur (S), silicon (Si), chromium (Cr), zinc (Zn), and calcium (Ca) elemental maps.

containing phases are also present (Supplementary Fig. 9a and Supplementary Table 4), which requires further thorough clarification by synchrotron-assisted crystallography investigations.

It is noteworthy that the patterns of metal acquisition of this archaeon grown on the genuine Martian mineral material differ substantially from our recently reported observations of its growth on the ordinary chondrite NWA 1172⁴¹. Encrustation with the thick Fe(Mn, Al)/P-outer layer with P solely represented in this layer, intracellular formation of crystalline phases of Fe, Mn oxides, and mixed Mn silicates are distinguishable features of growth on the Noachian Martian breccia. In the case of NWA 1172, our TEM observations showed that the encrusted cell remnants and iron-bearing accumulations on the cell surface of *M. sedula* have an amorphous structure, with a mixture of different amorphous iron-oxides/hydroxides⁴¹. A similar encrustation of the cell surface, but of a simpler, homogenous and not complex nature, was observed earlier for *M. sedula* cultivated on metal-containing terrestrial materials^{43,52}. When cells of *M. sedula* are grown on terrestrial minerals (e.g., tungsten mineral scheelite), then they are prone to encapsulation with homogenous

crystalline tungsten-harboring nanolayers deposited over the microbial cell surface⁴³. The observed multifaceted and complex biomineralization patterns of *M. sedula* grown on the Noachian breccia NWA 7034 can be well stated by rich, diverse mineralogy and multimetallic nature of this ancient Martian meteorite. The drastic difference between the biomineralization patterns of NWA 7034- and NWA 1172-grown cells of *M. sedula* emphasizes the importance of experiments on genuine Martian materials for Mars-relevant astrobiological investigations.

Organometallic fingerprints. Further geochemical analysis of the biologically mediated alteration of the meteorite material was performed by investigating microbial fingerprints left on the Noachian breccia NWA 7034. Electron paramagnetic resonance (EPR) measurements were implemented to identify paramagnetic species of transition metal ions (e.g., Fe) in the NWA 7034 sample and to investigate the impact of *M. sedula* on their paramagnetic centers, as well as to identify possible newly formed paramagnetic complexes and reactive intermediates in the biologically

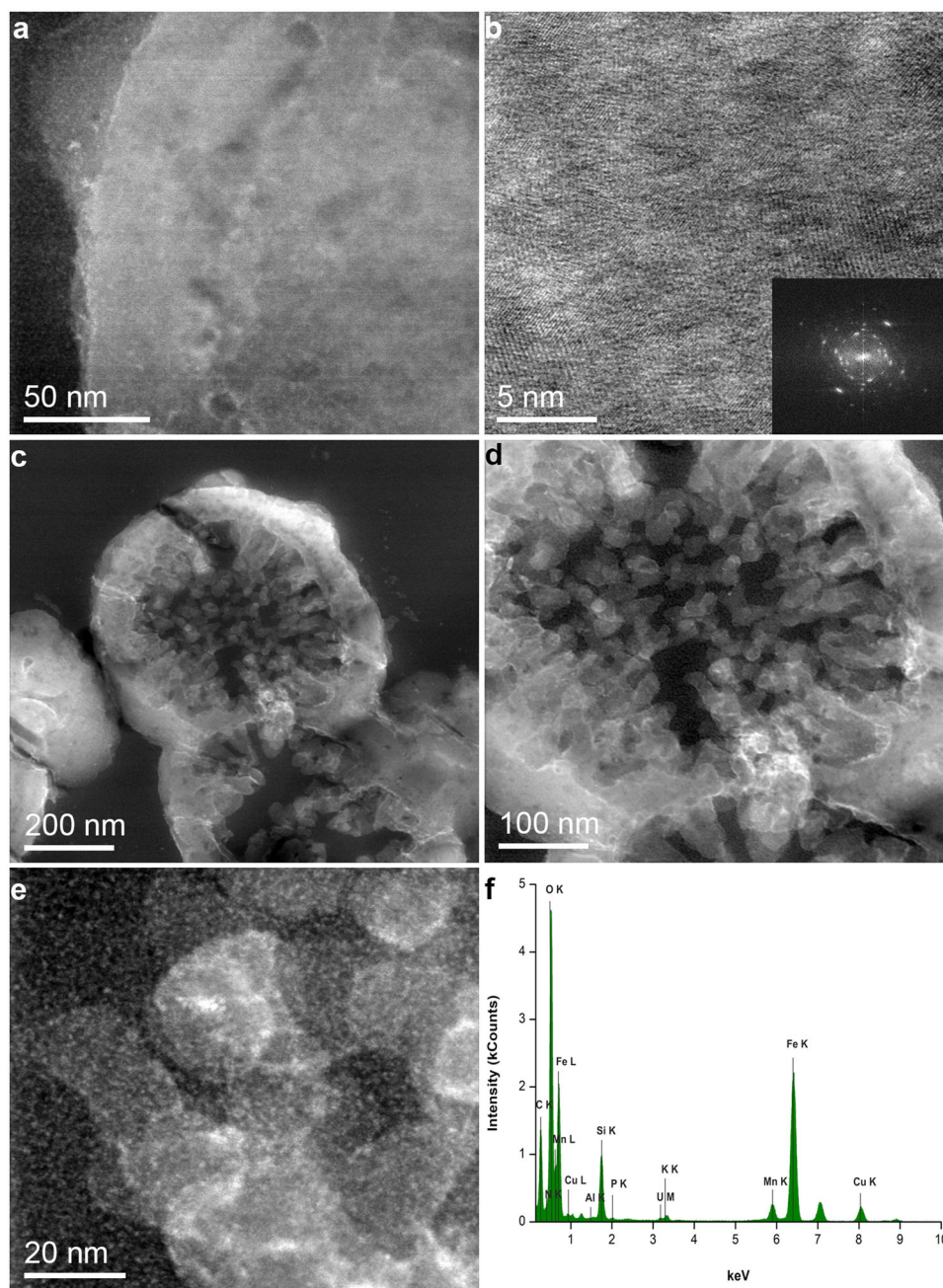


Fig. 3 High-resolution STEM (HR-STEM) analysis of *M. sedula* grown on NWA 7034. a, b Representative HR-STEM images of biogenic mineral deposits on the outer layer of *M. sedula* cell. Inset in panel (b) represents the fast fourier transform (FFT) pattern consistent with the phases of Fe, Mn, Al phosphates listed in Supplementary Tables 3 and 4. **c** The HAADF-STEM image of *M. sedula* cells. **d** Magnified HAADF-STEM image showing the amorphous blade-shaped structures protruding cellular environment. **e** The HR-STEM image of the intracellular amorphous nanoassemblies. **f** Energy-dispersive X-ray (EDS) spectra acquired from the nanometer-sized near-spherical aggregates in panel (e). Cu peaks in EDS spectra are due to the TEM grid and U peak is due to the staining solution.

processed NWA 7034. The EPR spectra obtained from raw, abiotic, and biogenic NWA 7034 samples were characterized by a signal with a broad linewidth (Supplementary Fig. 11), which might refer to multiple ionic paramagnetic species. Bio-transformation of the Noachian breccia NWA 7034 after the exposure to *M. sedula* resulted in a shifted g -value 2.93 at 273 K, compared to the raw and abiotically treated NWA 7034 material (g -values = 3.58/3.24, Supplementary Fig. 11). Low-spin ferric heme EPR resonances with highly specific g -values ~ 2.9 are assigned to heme ligated axially by an imidazole ligand of the proximal histidine, bound to the iron with Fe–N distances in

respiratory enzymes such as cytochromes^{58,59}. A group of microbial heme-containing enzymes are characterized by this distinctive spectral feature of g -values = 2.93^{58–62}. These enzymes have been indicated as playing a role in electron transfer linked to energy-yielding processes in various chemolithotrophs, including *M. sedula*^{44,56,57}, and most likely their heme prosthetic group contributes to a broad signal at $g = 2.93$ detectable solely after biotransformation of NWA 7034 (Supplementary Fig. 11). Heme-containing geoporphyrins can be resistant to degradation over long periods of time⁶³, for instance, in geological context of ~ 500 Ma-old oil shales⁶⁴. Abiotically formed ancestors of heme-

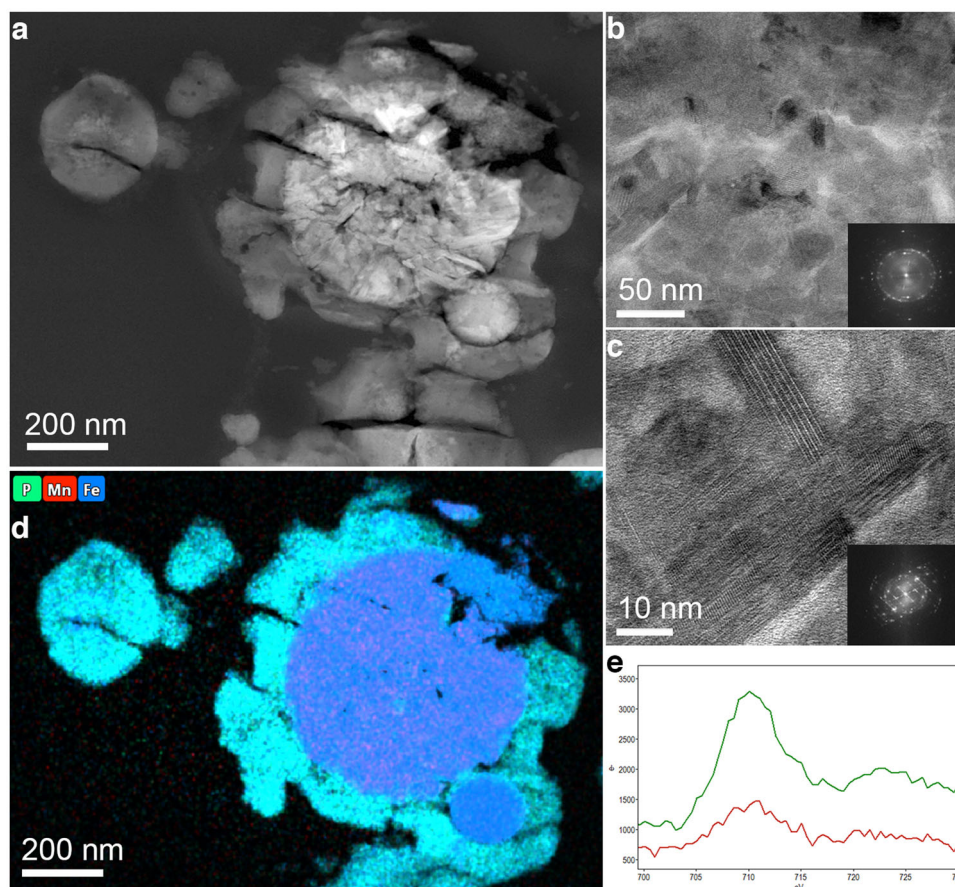


Fig. 4 Nanoanalytical spectroscopy investigations of *M. sedula* grown on NWA 7034. **a** The HAADF-STEM image of a cell of *M. sedula* used for high-resolution investigations and electron energy loss spectroscopy (EELS) analysis. **b, c** Representative HR-STEM of biogenic crystalline mineral deposits inside the cell of *M. sedula*. Insets in panels represent the fast fourier transforms (FFTs) consistent with the phases of tetragonal Mn_3O_4 -type nanoassemblages embedded into Fe_3O_4 . **d** EDS false colors composed mineral map of a cell of *M. sedula* (Mn-red, P-green, Fe-blue). The next mineral phases can be visualized: intracellular mixture of Mn-bearing phases (Mn_3O_4 , mixed $\text{Mn}_x\text{Si}_y\text{O}_z$ -containing phases (magenta); intracellular Fe-bearing phase Fe_3O_4 (blue); and mixed Fe, Mn, Al phosphates in the outer crust layer (cyan). Corresponding inter-atomic spacing (*d*-values) are presented in Supplementary Table 4. **e** Corresponding Fe $L_{2,3}$ -edge in the EELS acquired from the crust outer layer (shown as red line) and the intracellular nanocrystalline deposits (shown as green line) of the *M. sedula* cell.

containing porphyrins could have accumulated in primordial rock pools⁶⁵. The extreme stability of certain heme-containing fossils (e.g., geoporphyrins) makes them attractive targets for the search of extinct life on Mars. However, care must be taken in distinguishing their biogenicity from abiotically formed heme-containing compounds, e.g., abiotic porphyrins⁶⁶.

Fourier-transform infrared (FT-IR) spectroscopy data of the biotransformed NWA 7034 depicted several bands, which can be assigned to the vibration of functional S-containing aromatic organic groups^{67,68} and contribute toward thiophene-bearing respiratory quinones in plasma membranes of *M. sedula* (Fig. 5). The unique C_{30} isoprenoid quinones of sulfur metabolizing acidophilic chemolithotrophs of the archaeal order *Sulfolobales* (including *M. sedula*) are S-bearing aromatic derivatives of benzo-[b]-thiophen-4,7-quinone (see chemical formulas in Fig. 5), which function as electron carriers in the respiratory chains of these microorganisms^{69,70}. These quinones comprise 0.28–0.38% of cell dry weight and represent ancestral biomarkers in terrestrial marine environments⁷¹. Notably, recent Sample Analysis at Mars (SAM) measurements onboard the Curiosity rover detected thiophenic organic sulfur in ~3.5-Gyr (billion year)-old Murray formation, Gale crater⁴. These measurements did not reveal the exact source of thiophenic sulfur in the Murray formation. Both biogenic and abiotic origin could account for possible sources of

S-bearing thiophenes on Mars. Apart from sulfurization of organic molecules over geological time, presence of S-bearing refractory organic matter in meteorite material, interplanetary dust particles, and abiotic organic constituents of igneous rocks, S-bearing respiratory quinones as metabolic fingerprints of *M. sedula* or similar archaea can also represent potential thiophene sources. Sulfurization appears to be a plausible mechanism to preserve Martian organic matter and to keep it detectable and stable under destructive environmental conditions in 3-Gyr-old mudstones at Gale crater⁴. S-bearing thiophenes of *Sulfolobus* quinones might be targeted as specific refractory organic biomarkers with a promising preservation potential. To enable detection by spacecraft instrumentation in a natural Martian environment, a non-destructive biomarker analysis should be considered in order to yield the fine chemical and structural features of potential biomarkers (e.g., long aliphatic side chains of S-bearing thiophenes from *Sulfolobus* quinones). This is an important part for assessing the biogenicity of identified organic compounds (e.g., pyrolysis-GC-MS-based destructive analysis cannot yield intact molecules of thiophene-bearing quinones, but only residual thiophenes).

The presented investigations on Martian meteorite biogeochemistry motivate further experimental and theoretical work to build a detailed understanding of the full functional setup of

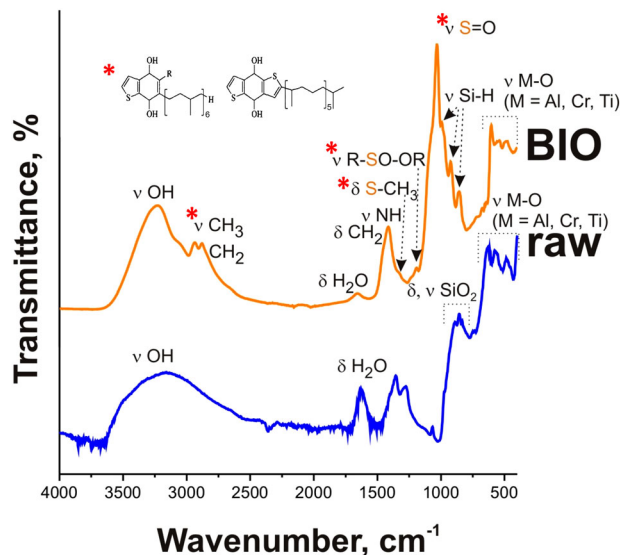


Fig. 5 FT-IR spectra of raw (blue) and biotransformed by *M. sedula* (orange) Noachian Martian breccia NWA 7034 in the region 4000–500 cm^{-1} . Spectral features highlighted with red asterisk contribute toward the S-bearing thiophenes of *Sulfolobales* quinones (thiopheno-benzo-quinones represented by general formulas): absorbance peak at 1083 cm^{-1} (S = O stretching of thiophenes); 1191 cm^{-1} (stretching vibrations of thiophenic R-SO-OR or RO-SO-OR); 1321 cm^{-1} (S-CH₃ stretching of methylated sulfuric species); 1031 cm^{-1} and 3056 cm^{-1} (stretching vibrations of hydrogen bonded C-H in aromatic thiophenes); spectral intensities at 1454 cm^{-1} and from 2800 to 3000 cm^{-1} (CH₂ of lipids, isoprenoid chains of thiopheno-benzo-quinones). Spectra analysis was performed using reference database^{67,68} and online database tool (http://www.chem.msu.ru/rus/teaching/tarasevich/Tarasevich_IR_tables_29-02-2012.pdf).

putative life based on inorganic sources available on Mars. Environmental settings on early Mars closely resembled those on early Earth with the conditions permissive for life to originate. In contrast to the current Mars conditions, bodies of liquid water, warmer temperature, and higher atmospheric pressure could have existed in Mars' early history over time scales comparable to the origin of life on Earth²¹. The period of moist surface conditions on Noachian Mars may have corresponded to the time during which life originated on Earth. Later on, starting from early Hesperian onwards, Mars lost most of its dense CO₂ atmosphere and liquid water and harsh surface conditions prevailed for ca. 3.5 Ga. The cold climate, the apparent absence of plate tectonic activity and fluvial alterations, and the absence of oxygen on Hesperian and Amazonian Mars indicate that the (sub-)surface Noachian paleoenvironments are potentially preserved in the rock record on a billion-year time scale^{21,72,73}. Several additional factors influence biosignature preservation in the rock record over geological time, e.g., rapidity of burial and mineral encapsulation of microbial cell^{74,75}. When cells are rapidly encrusted in massive mineral precipitates (Figs. 2, 3 and Supplementary Figs. 4, 5) and subsequently rapidly buried in mineral sediments, they may form lithified biological materials, which are long-lived in geological environments. These structures form textural or morphologic biosignatures that can be preserved in the geologic record^{74,75}. Furthermore, in Mars paleoenvironments anoxic conditions have been maintained⁷⁶ that restrict the oxidative destruction of organic matter and permit its preservation in the rock record at subsurface depth below the reach of other long-term harsh oxidizing factors, such as cosmic radiation^{74,75,77}. If life evolved on Mars, the traces of fossil evidence of the earliest Martian

biosphere may be well accessible in subsurface sediments. This has important implications for the exploration of past Martian habitability and potential Martian returned samples. The heavily Fe_nMn_xAl_yP_z-encrusted cells with intracellular crystalline deposits of cubic Fe₃O₄, tetragonal Mn₃O₄, and mixed Mn₂Si₂O₇ phases, described in the present study, may constitute relevant putative biosignatures to be explored in the Martian geological record, if they persist destructive environmental conditions in reference to geologic timescales. We propose further focus on microbial nano-lithologies and metalloorganic signatures of the chemolithotrophs, including nanoscale metal-microbial interfaces and S-bearing specific organic biomarkers (thiophenes from *Sulfolobales* quinones). The present study considers thermoacidophilic microbial fingerprints on Martian mineral material which are relevant for potential hydrothermal spring settings on Mars. Further work should be conducted with Martian relevant mineral materials (e.g., Martian meteorites and Mars regolith analogs) for a wide variety of other chemolithotrophs, as other niches for the origin of life on Mars (e.g., psychrophilic ancestral phenotype relevant for low-temperature lacustrine settings) may certainly not be excluded. The nanoscale interfaces of chemolithotrophs grown on Martian materials should be further comprehensively investigated with advanced synchrotron-assisted spectroscopic techniques. These investigations may provide a guiding point for in situ measurements to analyze collected Mars samples. Furthermore, the performed studies may pave the way to the efficient nanoanalytical spectroscopy of collected and returned Mars samples in order to assess their potential biogenicity.

Methods

Experimental design. *M. sedula* (DSMZ 5348) was cultivated in DSMZ88 *Sulfolobus* medium consisting of 1.3 g (NH₄)₂SO₄, 0.28 g KH₂PO₄, 0.25 g MgSO₄·7 H₂O, 0.07 g CaCl₂·2 H₂O, and 0.02 g FeCl₃·6 H₂O dissolved in 1 L of water. With subsequent autoclaving, Allen's trace elements solution was added to 1 L media resulting in 1.80 mg MnCl₂·4 H₂O, 4.50 mg Na₂B₄O₇·10 H₂O, 0.22 mg ZnSO₄·7 H₂O, 0.05 mg CuCl₂·2 H₂O, 0.03 mg Na₂MoO₄·2 H₂O, 0.03 mg VSO₄·2 H₂O, and 0.01 mg CoSO₄ final concentration. The pH was adjusted to 2.0 with 10 N H₂SO₄. Chemolithotrophic cultivation of *M. sedula* was conducted as described before⁴¹ in 200 mL glassblower modified Schott-bottle bioreactors (Duran DWK Life Sciences GmbH, Wertheim/Main, Germany), equipped with a thermocouple connected to magnetic stirring and a heating plate (IKA RCT Standard/IKA C-MAG HS10, Lab Logistics Group GmbH, Meckenheim, Germany) in order to control agitation and temperature. The bioreactors were equipped with three 5 mL graduated glass pipettes, permitting carbon dioxide and air gassing and sampling of culture, respectively. The graduated pipettes used for gassing were attached by silicon tubing to sterile 0.2 μm filters (Millex-FG Vent filter unit, Millipore, Billerica, USA). A Luer-lock system was attached to the sampling graduated pipettes to operate sampling with sterile syringes (Soft-Ject, Henke Sass Wolf, Tuttlingen, Germany). A water-cooled condenser (Carl Roth, Karlsruhe, Germany) was used to force the off-gas to exit. Electronic thermocouple was used to control the temperature inside the bioreactors during the cultivations of *M. sedula* at 73 °C. For chemolithoautotrophic growth, cultures were supplemented with 1 g/L of the Noachian breccia NWA 7034 (Mile High Meteorites Collection, 2.4 g fragment, non-covered with fusion crust, provided by Matt Morgan, Colorado Geological Survey). The meteorite sample (2.4 g, Supplementary Fig. 1) was ground and temperature sterilized at 180 °C in a heating chamber for a minimum of 24 h prior to autoclaving at 121 °C for 20 min. Abiotic controls comprised of culture media supplemented with sterilized NWA 7034, but without *M. sedula* cells, were included in all experiments. Growth of cells was observed by means of phase contrast/epifluorescence microscopy and release of soluble metal ions. To visualize cells wiggling on solid particles, a modified "DAPI" (4'-6'-Diamidino-2-phenylindole) procedure^{37,41,43,52,78} was used for cell staining. The stained cells were observed and recorded with ProgRes[®] MF cool camera (Jenoptik) mounted on Nikon eclipse 50i microscope, equipped with F36-500 Bandpass Filter Set (ex, 377/50 nm; em, 447/60 nm).

Scanning transmission electron microscopy. Cells of *M. sedula* were collected at stationary phase and primary fixed as described earlier⁴¹ at 4 °C in a 1 M Na-Cacodylate buffer supplemented with 2.5% glutaraldehyde. Followed by primary fixation, cells were post-fixed for 2 h in 1% OsO₄. After thorough washing (three times with 2 × 0.1 M Na-cacodylate, 1x dH₂O) and subsequent dehydration by a gradual ethanol series (30%, 50%, 70%, 90%, abs., each step with an incubation time of 30 min), cells were centrifuged after each dehydration step for 30 min and

resuspended for the subsequent ethanol treatment. Resulting samples were embedded in Spurr Low Viscosity Resin (Electron Microscopy Sciences, USA) and polymerized at 60 °C for a minimum of 48 h. Semi- and ultrathin sectioning was conducted by means of a Reichert-Jung Ultracut E ultramicrotome, with 50–70 nm ultrathin sections, followed by their staining using uranyl-acetate (15 min), and deposited on 200 copper grid mesh coated with formvar/carbon (Agar Scientific, UK). Sample preparation of NWA 7034 for transmission electron microscopy has been performed by focused ion beam (FIB) sputtering using a FEI Quanta 3D FEG instrument, equipped with an electron column hosting a field-emission electron source and an ion column hosting a Ga-liquid metal ion source (LMIS). Sputtering progress has been monitored by electron beam (EB) induced secondary electron (SE) imaging at EB settings of 5 keV accelerating voltage. Before sputtering, a Pt layer (length × width × height = 8 μm × 3 μm × 3 μm) was deposited onto the NWA 7034 surface by applying FIB Pt deposition at 16 kV IB acceleration voltage. The deposited nanocrystalline Pt served as protection layer during subsequent preparation steps.

HR-STEM investigations were performed on a probe-corrected FEI Titan G2 60–300 (S/TEM) microscope with an X-FEG Schottky field-emission electron source operated at 60 and 300 kV (current of 150 pA, beam diameter below 1 Å in STEM mode). The microscope is equipped with a Super-X detector (Chemi-STEM technology, Thermo Fisher Scientific), comprised of a Dual EELS - Gatan Imaging Filter (GIF) Quantum and four separate silicon drift detectors. Two different high-angle annular dark-field detectors (HAADF) and one annular dark-field (ADF) detector were applied to acquire the scanning transmission micrographs. Analytical investigations were performed using EDS and EELS carried out with a 19.7 and 20.5 mrad convergence and collection semiangles, respectively,^{79–81}. Spectrum images were collected for different areas/locations of *M. sedula* cells. For each investigated spot, elemental maps were extracted from EELS and EDS spectrum images^{41,43,52}. Afterwards, EELS and EDS spectra from investigated areas on the cell surface and inside of the cells were acquired/extracted. The acquired images and EELS spectra were processed via Gatan's Digital Micrograph being corrected for dark current and gain variations. EDS spectrum images were acquired and processed by using the VELOX software (Thermo Fisher Scientific).

The high-resolution STEM (HR-STEM) micrographs were processed by fast Fourier transformation (FFT) in order to measure the *hkl* distances in a certain orientation of the polycrystalline structures. The transmitted and the diffracted electrons passing through a specimen and satisfying the Bragg condition, are focused at the back focal plane of the objective lens and form the electron diffraction pattern. In this plane, the space where the electron diffraction pattern can be observed is called the reciprocal space, which is mathematically given by the Fourier transform of the real space. The Fourier transform of an image is therefore its frequency-domain representation⁸². The interplanar distances in a certain orientation of a crystal are specific for each crystal with given lattice parameters. The *hkl*-*d*-values are directly measured on the HR-STEM images or using the FFT images which display the frequencies spots corresponding to the inverse of the interplanar distance. The advantage of using this method is the identification of even nanocrystals of dimensions smaller than 5 nm or atomic clusters of 2–3 nm (if ordered). The FFT measured *d*-values (*hkl*) have then been compared with the possible phases extracted from the ICSD database (<https://icsd.fiz-karlsruhe.de>) and their calculated *d*-values (*hkl*)^{83–96}.

Infrared (IR) spectroscopy. IR spectra were recorded on a freeze-dried mineral-cell pellet, obtained from the liquid culture, using a FT-IR spectrometer (Bruker Optik GmbH) equipped with an MCT-detector (32 scans, resolution 4 cm⁻¹). Spectra analysis was performed using reference database^{67,68}.

Electron paramagnetic resonance spectroscopy. The EPR spectra were measured as described earlier³⁴ on an X-Band Bruker Elexsys-II E500 CW-EPR spectrometer (Bruker Biospin GmbH, Rheinstetten, Germany) at 90 ± 1 and 293 ± 1 K using a high-sensitivity cavity (SHQE1119). Solid-state EPR measurements were conducted using microwave frequency settled to 9 GHz, center field to 6000 G, modulation frequency to 100 kHz, sweep width to 12,000 G, sweep time to 335.5 s, microwave power to 15 mW, modulation amplitude to 20.37 G, resolution to 4096 points, and conversion time to 81.92 ms. The samples were loaded in EPR quartz tubes (Wilma-LabGlass, Vineland, NJ, USA) and scanning was performed three times, resulting to the average which was used for analysis. The spectrum of an empty control tube was subtracted from all sample spectra. The analysis of all spectra was performed using the Bruker Xep software.

Metal analysis. To determine the extracellular concentrations of soluble metal ions mobilized from NWA 7034 meteoritic material, culture samples were pre-clarified by centrifugation. Resulting pre-clarified samples of the culture supernatants were filtered via 0.44 μm pore size filters and subsequently analyzed by ICP-MS, Perkin Elmer ELAN 6100.

Data availability

All data are available in the main text, the Supplementary Information, and data repository Figshare (<https://doi.org/10.6084/m9.figshare.13574423>).

Received: 5 June 2020; Accepted: 18 January 2021;

Published online: 19 February 2021

References

- Grotzinger, J. P. et al. A habitable fluvio-lacustrine environment at Yellowknife Bay, Gale crater, Mars. *Science* **343**, 1242777 (2014).
- Hurwitz, J. A. et al. Redox stratification of an ancient lake in Gale crater, Mars. *Science* **356**, eaah6849 (2017).
- Blamey, N. J. F. et al. Evidence for methane in Martian meteorites. *Nat. Commun.* **6**, 7399 (2015).
- Eigenbrode, J. L. et al. Organic matter preserved in 3-billion-year-old mudstones at Gale crater, Mars. *Science* **360**, 1096–1101 (2018).
- Fairén, A. G. et al. Noachian and more recent phyllosilicates in impact craters on Mars. *Proc. Natl. Acad. Sci. USA* **107**, 12095–12100 (2010).
- Fraeman, A. A. et al. The stratigraphy and evolution of lower Mount Sharp from spectral, morphological, and thermophysical orbital data sets. *J. Geophys. Res. Planets* **121**, 1713–1736 (2016).
- Bishop, J. L. et al. Phyllosilicate diversity and past aqueous activity revealed at Mawrth Vallis, Mars. *Science* **321**, 830–833 (2008).
- Ehlmann, B. L. et al. Orbital identification of carbonate-bearing rocks on Mars. *Science* **322**, 1828–1832 (2008).
- Mustard, J. F. et al. Hydrated silicate minerals on Mars observed by the Mars Reconnaissance Orbiter CRISM instrument. *Nature* **454**, 305–309 (2008).
- Chevrier, V., Poulet, F. & Bibring, J. P. Early geochemical environment of Mars as determined from thermodynamics of phyllosilicates. *Nature* **448**, 60–63 (2007).
- Moser, D. E. et al. Decline of giant impacts on Mars by 4.48 billion years ago and an early opportunity for habitability. *Nat. Geosci.* **12**, 522–527 (2019).
- Bristow, T. F. et al. The origin and implications of clay minerals from Yellowknife Bay, Gale crater, Mars. *Am. Mineral.* **100**, 824–836 (2015).
- Vaniman, D. T. et al. Mineralogy of a mudstone at Yellowknife Bay, Gale crater, Mars. *Science* **343**, 1243480 (2014).
- Farquhar, J., Savarino, J., Jackson, T. L. & Thieme, M. H. Evidence of atmospheric sulphur in the Martian regolith from sulphur isotopes in meteorites. *Nature* **404**, 50–52 (2000).
- Weiss, M. C. et al. The physiology and habitat of the last universal common ancestor. *Nat. Microbiol.* **1**, 16116 (2016).
- Morrison, P. R. & Mojszisz, S. J. Tracing the early emergence of microbial sulfur metabolisms. *Geomicrobiol. J.* **38**, 1–21 (2020).
- Camprubi, E., Jordan, S. F., Vasiladiou, R. & Lane, N. Iron catalysis at the origin of life. *IUBMB Life* **69**, 373–381 (2017).
- Wächtershäuser, G. Pyrite formation, the first energy source for life: a hypothesis. *Syst. Appl. Microbiol.* **10**, 207–210 (1988).
- Wächtershäuser, G. Evolution of the first metabolic cycles. *Proc. Natl. Acad. Sci. USA* **87**, 200–204 (1990).
- Claessens, N. et al. Harnessing the power of microbial autotrophy. *Nat. Rev. Microbiol.* **14**, 692–706 (2016).
- McKay, C. P. & Stoker, C. R. The early environment and its evolution on Mars: implication for life. *Rev. Geophys.* **2**, 189–214 (1989).
- Schulze-Makuch, D. et al. Exploration of hydrothermal targets on Mars. *Icarus* **189**, 308–324 (2007).
- Bridges, J. C. & Schwenzer, S. P. The nakhlite hydrothermal brine on Mars. *Earth Planet. Sci. Lett.* **359–360**, 117–123 (2012).
- Schwenzer, S. P. et al. Gale crater: formation and post-impact hydrous environments. *Planet. Space Sci.* **70**, 84–95 (2012).
- Chatzitheodoridis, E., Haigh, S. & Lyon, I. A conspicuous clay ovoid in Nakhla: evidence for subsurface hydrothermal alteration on Mars with implications for astrobiology. *Astrobiology* **14**, 651–693 (2014).
- Michalski, J. R., Dobre, E. Z. N., Niles, P. B. & Cuadros, J. Ancient hydrothermal seafloor deposits in Eridania basin on Mars. *Nat. Commun.* **8**, 15978 (2017).
- Ruff, S. W. & Farmer, J. Silica deposits on Mars with features resembling hot spring biosignatures at El Tatio in Chile. *Nat. Commun.* **7**, 13554 (2016).
- Ruff, S. W., Campbell, K. A., Van Kranendonk, M. J., Rice, M. S. & Farmer, J. D. The case for ancient hot springs in Gusev crater, Mars. *Astrobiology* **20**, 475–499 (2020).
- McCubbin, F. M. et al. Geologic history of Martian regolith breccia Northwest Africa 7034: evidence for hydrothermal activity and lithologic diversity in the Martian crust. *J. Geophys. Res. Planets* **121**, 2120–2149 (2016).
- Hu, S. et al. NanoSIMS analyses of apatite and melt inclusions in the GRV 020090 Martian meteorite: hydrogen isotope evidence for recent past underground hydrothermal activity on Mars. *Geochim. Cosmochim. Acta* **140**, 321–333 (2014).
- Ehlmann, B. et al. Subsurface water and clay mineral formation during the early history of Mars. *Nature* **479**, 53–60 (2011).

32. Michalski, J. et al. Groundwater activity on Mars and implications for a deep biosphere. *Nature Geosci* **6**, 133–138 (2013).
33. Akanuma, S. et al. Experimental evidence for the thermophilicity of ancestral life. *Proc. Natl. Acad. Sci. USA* **110**, 11067–11072 (2013).
34. Stetter, K. O. Hyperthermophiles in the history of life. *Philos. Trans. R. Soc. Lond. B* **361**, 1837–1842 (2006).
35. González-Toril, E., Martínez-Frías, J., Gómez, J. M., Rull, F. & Amils, R. Iron meteorites can support the growth of acidophilic chemolithoautotrophic microorganisms. *Astrobiology* **5**, 406–414 (2005).
36. Gronstal, A. et al. Laboratory experiments on the weathering of iron meteorites and carbonaceous chondrites by iron-oxidizing bacteria. *Meteorit. Planet. Sci.* **44**, 233–247 (2009).
37. Kölbl, D. et al. Exploring fingerprints of the extreme thermoacidophile *Metallosphaera sedula* grown on synthetic Martian regolith materials as the sole energy sources. *Front. Microbiol.* **8**, 1918 (2017).
38. Tait, A. W., Gagen, E. J., Wilson, S. A., Tomkins, A. G. & Southam, G. Microbial populations of stony meteorites: substrate controls on first colonizers. *Front. Microbiol.* **8**, 1227 (2017).
39. Steele, A. et al. Investigations into an unknown organism on the Martian meteorite Allan Hills 84001. *Meteorit. Planet. Sci.* **35**, 273–241 (2000).
40. Benzerara, K., Menguy, N., Guyot, F., Dominici, C. & Gillet, P. Nanobacteria-like calcite single crystals at the surface of the Tataouine meteorite. *Proc. Natl. Acad. Sci. USA* **100**, 7438–7442 (2003).
41. Milojevic, T. et al. Exploring the microbial biotransformation of extraterrestrial material on nanometer scale. *Sci. Rep.* **9**, 18028 (2019).
42. Huber, G., Spinnler, C., Gambacorta, A. & Stetter, K. O. *Metallosphaera sedula* gen. and sp. nov. represents a new genus of aerobic, metal-mobilizing, thermoacidophilic Archaeobacteria. *Syst. Appl. Microbiol.* **12**, 38–47 (1989).
43. Blazevic, A. et al. Biotransformation of scheelite CaWO₄ by the extreme thermoacidophile *Metallosphaera sedula*: tungsten-microbial interface. *Front. Microbiol.* **10**, 1492 (2019).
44. Mukherjee, A., Wheaton, G. H., Blum, P. H. & Kelly, R. M. Uranium extremophily is an adaptive, rather than intrinsic, feature for extremely thermoacidophilic *Metallosphaera* species. *Proc. Natl. Acad. Sci. USA* **109**, 16702–16707 (2012).
45. Nyquist, L. E. et al. Rb-Sr and Sm-Nd isotopic and REE studies of igneous components in the bulk matrix domain of Martian breccia Northwest Africa 7034. *Meteorit. Planet. Sci.* **51**, 483–498 (2016).
46. Cassata, W. S. et al. Chronology of Martian breccia NWA 7034 and the formation of the Martian crustal dichotomy. *Sci. Adv.* **4**, eaap8306 (2018).
47. Agee, C. B. et al. Unique meteorite from early Amazonian Mars: water-rich basaltic breccia Northwest Africa 7034. *Science* **339**, 780–785 (2013).
48. McSween, H. Y., Taylor, G. J. & Wyatt, M. B. Elemental composition of the Martian crust. *Science* **324**, 736–739 (2009).
49. Beck, P. et al. A Noachian source region for the “Black Beauty” meteorite, and a source lithology for Mars surface hydrated dust? *Earth Planet. Sci. Lett.* **427**, 104–111 (2015).
50. Kish, A. J. et al. Preservation of archaeological surface layer structure during mineralization. *Sci. Rep.* **25**, 26152 (2016).
51. Humayun, M. et al. Origin and age of the earliest Martian crust from meteorite NWA 7533. *Nature* **503**, 513–516 (2013).
52. Milojevic, T. et al. Nanoscale tungsten-microbial interface of the metal immobilizing thermoacidophilic archaeon *Metallosphaera sedula* cultivated with tungsten polyoxometalate. *Front. Microbiol.* **10**, 1267 (2019).
53. Johnson, T. B. et al. Secretion and fusion of biogeochemically active archaeal membrane vesicles. *Geobiology* **00**, 1–15 (2018).
54. Fleet, M. E. The structure of magnetite. *Acta Crystallogr. B* **37**, 917–920 (1981).
55. Jarosch, D. Crystal structure refinement and reflectance measurements of hausmannite, Mn₃O₄. *Miner. Petrol.* **37**, 15–23 (1987).
56. Auernik, K. S. & Kelly, R. M. Identification of components of electron transport chains in the extremely thermoacidophilic crenarchaeon *Metallosphaera sedula* through iron and sulfur compound oxidation transcriptomes. *Appl. Environ. Microbiol.* **74**, 7723–7732 (2008).
57. Zeldes, B. M. et al. Determinants of sulphur chemolithoautotrophy in the extremely thermoacidophilic Sulfolobales. *Environ. Microbiol.* **21**, 3696–3710 (2019).
58. Cooper, C. E. & Salerno, J. C. Characterization of a novel g' = 2.95 EPR signal from the binuclear center of mitochondrial cytochrome c oxidase. *J. Biol. Chem.* **267**, 280–285 (1992).
59. Calhoun, M. W., Gennis, R. B. & Salerno, J. C. The formate complex of the cytochrome bo quinol oxidase of *Escherichia coli* exhibits a ‘g = 12’ EPR feature analogous to that of ‘slow’ cytochrome oxidase. *FEBS Lett.* **309**, 127–129 (1992).
60. Gudat, J. C., Singh, J. & Wharton, D. C. Cytochrome oxidase from *Pseudomonas aeruginosa*. I. Purification and some properties. *Biochim. Biophys. Acta* **292**, 376–390 (1973).
61. Pealing, S. L. et al. Spectroscopic and kinetic studies of the tetraheme flavocytochrome c from *Shewanella putrefaciens* NCIMB400. *Biochemistry*. **34**, 6153–6158 (1995).
62. Venceslau, S. S., Matos, D. & Pereira, I. A. EPR characterization of the new Qrc complex from sulfate reducing bacteria and its ability to form a supercomplex with hydrogenase and Tpc3. *FEBS Lett.* **585**, 2177–2181 (2011).
63. Callot, H. J. & Ocampo, R. Geochemistry of porphyrins. In *The Porphyrin Handbook* (eds. Kadish, K. M., Smith, K. M. and Guilard, R.) Vol. 1, 349–398 (Academic Press, 2000).
64. Serebrennikova, O. V. & Mozzhelina, T. K. Features of porphyrin compounds in Cambrian oil shales from Yakutiya, Siberia. *Org. Geochem.* **21**, 891–895 (1994).
65. Pleyer, H. L., Strasdeit, H. & Fox, S. A possible prebiotic ancestry of porphyrin-type protein cofactors. *Orig. Life Evol. Biosph.* **48**, 347–371 (2018).
66. Fox, S. & Strasdeit, H. A possible prebiotic origin on volcanic islands of oligopyrrole-type photopigments and electron transfer cofactors. *Astrobiology* **13**, 578–595 (2013).
67. Lin-Vien, D., Colthup, N. B., Fateley, W. G. & Grasselli, J. G. *Organic Sulfur Compounds* (Academic Press, 1991).
68. Larkin, P. *Infrared and Raman Spectroscopy: Principles and Spectral Interpretation* (Elsevier, 2011).
69. De Rosa, M. et al. Caldariellaquinone, a unique benzo[b]thiophen-4,7-quinone from *Caldariella acidophila*, an extremely thermophilic and acidophilic bacterium. *J. Chem. Soc. Perkin. Trans.* **16**, 653–657 (1977).
70. Thurl, S., Witke, W., Buhrow, I. & Schäfer, W. Quinones from Archaeobacteria, II. Different types of quinones from sulphur-dependent Archaeobacteria. *Biol. Chem. Hoppe Seyler.* **367**, 191–197 (1986).
71. Elling, F. J. et al. Respiratory quinones in Archaea: phylogenetic distribution and application as biomarkers in the marine environment. *Environ. Microbiol.* **2**, 692–707 (2016).
72. Grotzinger, J. P. & Milliken, R. E. The sedimentary rock record of Mars: distribution, origins, and global stratigraphy. In *Sedimentary Geology of Mars* (eds. Grotzinger, J. P. & Milliken, R. E.) 1–48 (SEPM Society for Sedimentary Geology, 2012).
73. Malin, M. C. & Edgett, K. S. Sedimentary rocks of early Mars. *Science* **290**, 1927–1937 (2000).
74. Hays, L. E. et al. Biosignature preservation and detection in mars analog environments. *Astrobiology* **4**, 363–400 (2017).
75. Westall, F. et al. Biosignatures on Mars: what, where, and how? Implications for the search for Martian life. *Astrobiology* **11**, 998–1029 (2015).
76. Sholes, S. F., Smith, M. L., Claire, M. W., Zahnle, K. J. & Catling, D. C. Anoxic atmospheres on Mars driven by volcanism: implications for past environments and life. *Icarus* **290**, 46–62 (2017).
77. Onstott, T. C. et al. Paleo-rock-hosted life on Earth and the search on Mars: a review and strategy for exploration. *Astrobiology* **19**, 1230–1262 (2019).
78. Huber, H., Huber, G. & Stetter, K. O. A modified DAPI fluorescence staining procedure suitable for the visualization of lithotrophic bacteria. *Syst. Appl. Microbiol.* **6**, 105–106 (1985).
79. Rienks, E. D. L. et al. Large magnetic gap at the Dirac point in Bi₂Te₃/MnBi₂Te₄ heterostructures. *Nature* **576**, 423–428 (2019).
80. Albu, M. et al. Self-organized Sr leads to solid state twinning in nano-scaled eutectic Si phase. *Sci. Rep.* **6**, 31635 (2016).
81. Goldstein, J. I., Williams, D. B. & Cliff, G. Quantification of energy dispersive spectra. In *Principles of Analytical Electron Microscopy* (eds. Joy, D. C., Romig, A. D. & Goldstein, J. I.) 155–217 (Plenum Press, 1986).
82. Williams, D. B. & Carter, C. B. *High-resolution TEM* (Springer, 2009).
83. Finklea, S. L., Cathey, L. & Amma, E. L. Investigation of the bonding mechanism in pyrite using the Mössbauer effect and X-ray crystallography. *Acta Crystallogr. A* **32**, 529–537 (1976).
84. Jin, S., Wang, X. & Xu, H. Revisiting the I $\overline{1}$ structures of high-temperature Ca-rich plagioclase feldspar—a single-crystal neutron and X-ray diffraction study. *Acta Crystallogr. B* **74**, 152–164 (2018).
85. Matsumoto, T., Tokonami, M. & Morimoto, N. The crystal structure of omphacite. *Am. Mineral.* **60**, 634–641 (1975).
86. Fleet, M. E. The structure of magnetite: defect structure II. *Acta Crystallogr. B* **38**, 1718–1723 (1982).
87. Yamanaka, T. Structural changes induced by lattice-electron interactions: SiO₂ stishovite and FeTiO₃ ilmenite. *J. Synchrotron. Radiat.* **12**, 566–576 (2005).
88. Henry, P. F., Weller, M. T. & Wilson, C. C. Determination of the cation distribution in Fe₂Ni(PO₄)₂ using isotopic substitution and powder neutron diffraction share. *J. Appl. Cryst.* **36**, 1361–1367 (2003).
89. Keller, P., Lissner, F. & Schleid, T. The crystal structure of stanekite, (Fe₃+, Mn₂+Fe₂+Mg)₂[PO₄]O, from Okatjimukuju, Karibib (Namibia), and its relationship to the polymorphs of synthetic Fe₂[PO₄]O. *Eur. J. Mineral.* **18**, 113–118 (2006).
90. Eventoff, W., Martin, R. & Peacor, D. R. The crystal structure of heterosite. *Am. Mineral.* **57**, 45–51 (1972).

91. Lightfoot, P. & Cheetham, A. K. Neutron diffraction study of the cation distributions in the systems $\text{Fe}_{7-x}\text{M}_x(\text{P O}_4)_6$ ($\text{M} = \text{Mn}$ or Co). *J. Chem. Soc. Dalton Trans.* **89**, 1765–1769 (1989).
92. Steele, I. M., Olsen, E., Pluth, J. J. & Davis, A. M. Occurrence and crystal structure of Ca-free beusite in the El Sarnal IIIA iron meteorite. *Am. Mineral.* **76**, 1985–1989 (1991).
93. Nord, A. G. & Ericsson, T. The cation distribution in synthetic $(\text{Fe}, \text{Mn})_3(\text{PO}_4)_2$ graftonite-type solid solutions. *Am. Mineral.* **67**, 826–832 (1982).
94. Giuseppetti, G. & Tadini, C. The crystal structure of childrenite from Tavistock (SW England), Ch89 Eo11 term of childrenite-eosphorite series. *Neues J. B. Miner. Mh.* **84**, 263–271 (1984).
95. Grey, I. E., MacRae, C. M., Keck, E. & Birch, W. D. Aluminium-bearing strunzite derived from jahnsite at the Hagendorf-Sud pegmatite, Germany. *Mineral. Mag.* **76**, 1165–1174 (2012).
96. Kopec, M. et al. Structural and magnetic properties of $\text{Li}_x(\text{Mn}_y\text{Fe}_{1-y})\text{PO}_4$ electrode materials for Li-ion batteries. *J. Power Sources* **189**, 1154–1163 (2009).

Acknowledgements

The authors gratefully acknowledge Chakib Djediat (Muséum National d'Histoire Naturelle, Paris) for the valuable help during the TEM sample preparation. We wish to thank Marc Pignitter (University of Vienna) for fruitful discussions and help with EPR analysis and Martina Dienstleder (Graz Centre for Electron Microscopy) for help with FIB preparation and anonymous reviewers for their valuable suggestions. This work was funded by the Austrian Science Fund (FWF) through an Elise-Richter Research Program V333 “Iron and Sulfur-oxidizing Machinery of the bioleaching Archaeon *Metallosphaera sedula*” to T.M. The STEM measurements partially received funding from the European Union’s Horizon 2020 research and innovation programme under grant agreement No. 823717 – ESTEEM3.

Author contributions

T.M., D.K., and M.A. performed experiments and analyzed the data. T.M., M.A., D.K., G.K., R.B., and M.M. provided editorial input, discussed the results, and contributed to the final manuscript. R.B. contributed to the literature search and critical revision of the

article. T.M. led, conceived, and designed the project, interpreted experiments, and wrote the manuscript.

Competing interests

The authors declare no competing interests.

Additional information

Supplementary information The online version contains supplementary material available at <https://doi.org/10.1038/s43247-021-00105-x>.

Correspondence and requests for materials should be addressed to T.M.

Peer review information Primary handling editor: Joe Aslin.

Reprints and permission information is available at <http://www.nature.com/reprints>

Publisher’s note Springer Nature remains neutral with regard to jurisdictional claims in published maps and institutional affiliations.



Open Access This article is licensed under a Creative Commons Attribution 4.0 International License, which permits use, sharing, adaptation, distribution and reproduction in any medium or format, as long as you give appropriate credit to the original author(s) and the source, provide a link to the Creative Commons license, and indicate if changes were made. The images or other third party material in this article are included in the article’s Creative Commons license, unless indicated otherwise in a credit line to the material. If material is not included in the article’s Creative Commons license and your intended use is not permitted by statutory regulation or exceeds the permitted use, you will need to obtain permission directly from the copyright holder. To view a copy of this license, visit <http://creativecommons.org/licenses/by/4.0/>.

© The Author(s) 2021